

1 **Resolving Northern Alaska Earthquake Sequences Using the**
2 **Transportable Array and Probabilistic Location Methods**

3

4 **Steven J. Gibbons** Norges Geotekniske Institutt, Oslo, Norway - steven.gibbons@ngi.no, @stevenjgibbons on Twitter

5 **Natalia A. Ruppert,** Alaska Earthquake Center, Geophysical Institute, University of Alaska Fairbanks, Fairbanks,
Alaska, U.S.A. <naruppert@alaska.edu>

6 **Ezgi Karasözen,** Alaska Earthquake Center, Geophysical Institute, University of Alaska Fairbanks, Fairbanks,
Alaska, U.S.A. <ezgikarasozen@gmail.com> @ezgikarasozen on Twitter

7 **Kasey Aderhold,** IRIS, Washington DC, USA. <kasey@iris.edu>; @KaseyAderhold on Twitter

8 **Ian Dickson** University of Colorado, Denver, Denver, USA. <iandickson1@gmail.com>
<[@IanJDickson](https://twitter.com/IanJDickson)> on Twitter

9

10

11 Corresponding author:

12

13 Steven J. Gibbons

14 Norges Geotekniske Institutt

15 Sognsveien 72

16 0855 Oslo

17 Norway

18 steven.gibbons@ngi.no

19

20

21

22

23

24 **ABSTRACT**

25 Between 2014 and 2017, almost 200 new seismic stations were installed in Alaska and northwestern
26 Canada as part of the EarthScope USArray Transportable Array (TA). These stations currently provide
27 an unprecedented capability for the detection and location of seismic events in regions with
28 otherwise relatively sparse station coverage. Two interesting earthquake sequences in 2018/2019 in
29 the north eastern Brooks Range were exceptionally well recorded due to this deployment. First is the
30 aftershock sequence of the M_w 6.4 and M_w 6.0 Kaktovik earthquakes of 12 August 2018, the largest
31 earthquakes recorded to-date in the region. The second is the Niviak swarm, southwest of the
32 Kaktovik sequence. Since July 2018, over 4000 earthquakes between magnitudes 1 and 4.3 have
33 been recorded across a region exceeding 5000 square kilometers. We explore how the Bayesloc
34 probabilistic multiple seismic event location algorithm can better resolve features of these two
35 sequences, exploiting the large numbers of readings that the improved station coverage provides
36 from events down to magnitudes below 2. The Bayesloc calculations consistently move events in the
37 Kaktovik sequence a few kilometers to the northeast, providing an almost linear ESE-striking
38 southern limit to the aftershock zone. Analysis of the Bayesloc joint probability distribution of
39 corrections to travel time predictions indicate that anomalously fast wave propagation to the
40 southwest is likely the most significant contribution to the seismic event mislocation. The joint
41 relocations are more consistent with InSAR-inferred coseismic displacement than the network
42 location estimates. The Bayesloc relocation of the Niviak events confirms that the earthquakes are
43 distributed between many distinct clusters of seismicity which have clearer spatial separation
44 following the relocation. The probabilistic relocations motivate both double-difference studies to
45 better resolve clustered seismicity at the smallest spatial scales and systematic multiple event
46 relocation studies to calculate structure and travel time corrections over larger scales.

47 INTRODUCTION

48 Between 2004 and 2015, the EarthScope USArray Transportable Array (TA) of ~400 digital broadband
49 seismometers was deployed from west to east across the "Lower 48" states, with stations remaining
50 in place for 1.5-2 years before being moved to a new location to the east. Deployment in Alaska and
51 northwest Canada began in 2014 after initial test installs, and the full network was operational by the
52 end of the 2017 field season. A comprehensive review of the deployment is provided by Busby and
53 Aderhold (2020). Whereas the permanent networks are concentrated in the most seismically active
54 regions of Alaska, the TA provides a remarkably uniform coverage of the remaining territory. Ruppert
55 and West (2020) discuss the lowering of the seismic detection thresholds that the additional stations
56 provide and draw attention to two extensive seismic sequences in the relatively aseismic regions,
57 which could only be characterized to the degree they are because of the TA presence. The first is the
58 aftershock sequence of the 12 August 2018 M_w 6.4 Kaktovik earthquake, the second is the 2018-
59 2019 Eastern Brooks Range sequence (Figure 1).

60 Seismicity in northeastern Alaska is distributed over a ~200-km-wide, ~500 km-long zone that trends
61 southwest to northeast. The northern limit of this zone extends into the Beaufort Sea, while its
62 southern end is truncated by the Tintina Fault, a major right-lateral strike slip fault that extends
63 eastward into Canada. Earthquakes have been recorded in this region since regional monitoring
64 began in the early 1970s (Gedney et al., 1977; Estabrook et al., 1988). Although the seismic record
65 until recently has been poor, moderate-sized earthquakes have been recorded in the region for
66 decades, albeit with highly variable accuracy. There has been one magnitude 5 or greater earthquake
67 every few years on average. The earthquakes have occurred throughout the entire region, generally
68 do not follow well-defined linear trends, and sometimes present swarm-like behavior for months to
69 years before returning to its previous state.

70 There are no mapped active faults between the Tintina fault to the south and the offshore faults in
71 the Beaufort Sea to the north (Koehler et al., 2012). Given the extensive seismicity in the area,

72 however, this apparent lack of active faults may be attributed to limited geologic field mapping,
73 which is due in large part to the remoteness of the area and the challenges this presents for
74 undertaking geologic mapping studies. Crustal seismicity of northeastern Alaska has long been
75 recognized as an earthquake hazard; it has been attributed to far-field deformation from the
76 subduction of the Pacific plate compounded by collision of the Yakutat block by a variety of studies
77 (e.g., Mazzotti and Hyndman, 2002; Leonard et al., 2008; Mazzotti et al., 2008).

78 Gaudreau et al. (2019) provide a thorough study of the August 2018 earthquake and aftershock
79 sequence both with seismological and InSAR data. They find that seismological location estimates of
80 the mainshock and numerous aftershocks are a few kilometers to the south of the InSAR-inferred
81 fault plane and discuss hypotheses for the discrepancy. These include the possibility of instrumental
82 timing errors, which could be significant given the unfavorable azimuthal station coverage. They
83 conclude that heterogeneous velocity structure in the crust is a more likely explanation. In this study
84 we try to resolve the issue by applying the Bayesloc probabilistic multiple-event location algorithm
85 (Myers et al., 2007) which has been shown to provide improved locations for clustered seismicity,
86 partly by mitigating the influence of velocity heterogeneity. This procedure provides both
87 probabilistic hypocenter and origin time estimates for the earthquakes and estimates of bias and
88 uncertainty in travel time predictions. We present Bayesloc relocations of earthquakes in both
89 sequences and provide justification as to why we can have confidence in the results.

90

91

92 **AFTERSHOCKS OF THE 12 AUGUST 2018, M_w 6.4 KAKTOVIK EARTHQUAKE**

93 Figure 2a) displays locations of events in the Alaska Earthquake Center (AEC) catalog likely to be
94 associated with the 12 August 2018 Kaktovik earthquake sequence, based on location and time.
95 Earthquakes in this catalog are located by automatic detection algorithms and later reviewed event-
96 by-event by human analysts who correct erroneous auto-picks and add more phase picks that the
97 auto-detectors may have missed. We apply Bayesloc, which locates multiple events simultaneously in
98 a probabilistic framework, to see if structure can be identified in the aftershock distribution not
99 found in the network locations. The motivation is that Bayesloc seeks a joint probability distribution
100 of all event hypocenters, origin times, arrival time uncertainty, and corrections to travel time
101 predictions, and may be able to compensate for geologic heterogeneity and consequent deficiencies
102 in the underlying velocity model used. In contrast, the network solutions are forced to assume zero-
103 mean Gaussian distributions for all uncertainties and are therefore unable to identify bias in any
104 parameters common to multiple events. Gibbons and Kväerna (2017) applied Bayesloc to the
105 aftershocks of the October 2005 Kashmir earthquake and found far more structured event clusters
106 than could be resolved in the single-event network solutions. In that case study, the primary cause of
107 mislocation in the network solutions was deemed likely to be anomalous travel times to stations at
108 regional distances. The probabilistic estimates for travel time corrections transformed the clouds of
109 aftershocks to align convincingly with the strike of the surface rupture. Bayesloc was applied by
110 Hayes et al. (2015) for accurate relocations of aftershocks from the Mw 7.8 April 2015 Gorkha
111 earthquake, Nepal, by Nealy et al. (2017) to constrain the 2008 Wells, Nevada, sequence, and by Pyle
112 et al. (2015) to provide accurate event locations for seismicity in Rock Valley, Nevada.

113 Whereas the relocation of the Kashmir aftershocks involved a significant repicking of arrivals from
114 raw waveform data, it is important to note here that all Bayesloc solutions presented use exactly the
115 same set of arrivals as the AEC network location estimates. A 1D velocity model was prescribed
116 based upon profiles presented in Fuis et al. (1997) and travel time tables were calculated for Pg, Pn,
117 Pb, Sg, Sn, Sb phases (see Storchak et al., 2003) for distances up to around 15 degrees, as applicable,

118 for input to the Bayesloc program. Additional travel time tables containing the travel time for the
119 first arriving P and first arriving S phase were also calculated and labelled P1 and S1. Following the
120 practice of Gibbons et al. (2017), relocating seismicity along the North Atlantic spreading ridge, we
121 performed a parallel calculation using a different basis velocity model (in this case AK135, Kennett et
122 al., 1995) to confirm that the final joint probability distribution of event hypocenters was largely
123 stable to small changes in the underlying 1D velocity model. As seen in Figure 1, there are stations
124 ranging from a few tens of kilometers to many hundreds of kilometers and so the identification of
125 the first arriving phase will change with distance. There may be uncertainty regarding the
126 identification of the first arriving phase in some regions. All first P and S arrivals from the AEC bulletin
127 were initially labelled P1 and S1 and we exploit the Bayesloc probabilistic identification of phase
128 labels (Myers et al., 2009) to attribute the most likely label to each arrival given the most probable
129 location.

130 Figure 2b) shows the distribution of mean event hypocenters from a run of Bayesloc with no priors
131 on the event locations and a total of 40000 iterations. The diffuse southern boundary of the network
132 solutions becomes a sharper edge with an ESE strike direction, a few kilometers north of the
133 southernmost epicenters from the AEC catalog. The contrast between the two sets of event locations
134 is more easily seen in Figure 2c) in which the relocations are plotted on top of the catalog location
135 estimates. The northern boundary of the aftershock cloud remains diffuse and largely unchanged in
136 the relocations. We display the surface projections of the InSAR-modelled western and eastern fault
137 segments from Gaudreau et al. (2019) in each of panels a), b) and c). In panel a), the network
138 location estimates almost all lie to the south of these two lines. In panel b), the southern extent of
139 the relocated events is approximately parallel to the western fault and the northern extent of the
140 relocated events is approximately parallel to the eastern fault. In Figure 2d) we illustrate how the
141 events in different regions of the aftershock zone are moved. Essentially all events are shifted in a
142 northeasterly direction. Events in the western part of the aftershock zone may be relocated more in
143 a northerly direction, and events in the eastern part of the aftershock zone in a more easterly

144 direction, although the pattern is quite consistent. The relocations obtained using the AK135 model
145 as a basis are essentially identical to those displayed in Figure 2.

146 In Figure 3 we display both the distance and direction of each relocation. The majority of the larger
147 events are relocated to the northeast by between 2 and 10 km. Events which are relocated in a
148 significantly different direction are low magnitude events and may be subject to far poorer location
149 constraints to begin with due to fewer phase-arrival readings and poorer azimuthal coverage. Figure
150 3 demonstrates that, whereas the overall change of shape of the aftershock cloud is significant, the
151 relocations of the individual events are modest. Given the station geometry, the relocated epicenters
152 lie well within the formal uncertainty ellipses of the AEC catalog locations. The elliptical distribution
153 of the relocation vector end-points provides an indication of consistency between the two sets of
154 location estimates. Whereas an identical set of phase arrival times is used to construct both sets of
155 origin estimates, the two location procedures are entirely independent; no information about the
156 catalog event locations is used as prior information for the Bayesloc calculation.

157

158

159

160

161

162

163 **VALIDATING AND INTERPRETING PROBABILISTIC EARTHQUAKE RELOCATIONS**

164 The underlying algorithm in Bayesloc is iterative. It is instructive to examine the progress of the
165 solution from start to end understand why the resulting pattern of hypocenter estimates may
166 provide a higher confidence image of the seismicity. The latitude, longitude, depth, and origin times
167 of the events, the uncertainties associated with the arrival time estimates, and corrections to the
168 travel time estimates for each of the arrivals form a large parameter space for a given input. The
169 Monte Carlo Markov Chains in the Bayesloc algorithm explore this parameter space to try to
170 converge to a solution which best supports the full set of observations. The process starts with no
171 knowledge of the true parameters (unless prior information is available and provided) and probes
172 stochastically through different alternatives, identifying favorable choices.

173 In Figure 4a) we see as plain white symbols the final mean epicenters of all the events. Superimposed
174 onto this image are the location estimates at each iteration for a single selected event, displayed as
175 small colored dots to indicate the iteration number. (Only the first 10000 iterations are displayed
176 since changes in the epicenter estimates do not change significantly beyond that number.) Blue dots
177 in Figure 4a) indicate trial epicenters for this event in the earlier iterations and red dots indicate trial
178 epicenters towards the end. The most important features in the model parameter space in the
179 presence of geologic or velocity structure heterogeneity are the corrections to travel time
180 predictions. Gibbons et al. (2017) demonstrated very large travel time residuals for individual
181 regional station-phase combinations that were consistent from event-to-event over wide
182 geographical regions: biases far larger than the uncertainty in the arrival time estimates themselves.
183 This is why we plot (in Figure 4b) the observed minus predicted travel time residual of a given phase
184 arrival at a given station for every hypocenter and origin time estimate for this event as a function of
185 the iteration number. The convergence (or otherwise) of this parameter, and the corresponding
186 parameters for other phase/station combinations, provides an indicator as to whether the process
187 has converged on a solution. This offers an insight into how the event locations might relate to local
188 velocity structure.

189 The station and phase combination displayed in Figure 4b) is the first P-arrival at station D25K, the
190 closest station southwest of the aftershock zone. Before describing the evolution of this time residual
191 with iteration number, it is worth taking the time to consider what values of this parameter would
192 imply about the velocity structure between the aftershock zone and this station. How would the
193 values be affected by an analyst reading error, or a clock error? If we assume that the analyst placed
194 the arrival time estimate very accurately, and that the instrumental time-stamp is correct, then a
195 zero value of the observed minus predicted travel time residual means that our baseline 1D velocity
196 model provides an accurate representation of the geologic structure along these paths. A negative
197 value of this residual would mean that the picked arrival time is before the predicted arrival time,
198 and therefore that the seismic waves travel faster along the path than the model predicts. Similarly, a
199 positive value would imply slower rock than the model predicts. If the analyst placed the arrival time
200 estimate too late on the seismogram, this would move the curve up uniformly; this offset would be
201 constant for all hypocenter and origin time estimates. A too-early arrival time estimate would move
202 the curve down uniformly. We have a corresponding curve for every event in our dataset for which a
203 first P-arrival at station D25K has been picked: potentially several thousand such curves. The travel
204 time prediction correction for this phase and station combination, as part of the final joint probability
205 distribution, would consider all the curves generated. A timing error on the station would lift the P-
206 and S- time residuals for the station up or down by the same amount. It is important to note that the
207 earthquakes relocated in these two sequences occurred over time-intervals of many months (see
208 Ruppert and West, 2020, for details). A timing error typically covers a limited time-span, or is very
209 variable with time, and would likely be detected.

210 At the very start of the Bayesloc run, the time-residual in Figure 4b) takes on extreme values (often
211 greatly exceeding the actual travel time from the true event location to the station) as the trial
212 hypocenters and origin times for the event lie far from the true values. Few iterations pass before
213 epicenter estimates begin to stabilize in the region of the map where the blue dots in Figure 4a) are
214 observed. The time-residuals in Figure 4b) oscillate around a mean value of around

215 -0.8 seconds. At iteration 1000, corrections to model-based travel time predictions are activated
216 within Bayesloc. At this point, a rapid change in the evolution of this travel time-residual is observed,
217 decreasing to around -2 seconds. The corresponding trial hypocenters move northeast. A more
218 negative observed minus predicted time-residual means that the seismic wavefront is travelling
219 further than the basis model expects in a given time, and the event hypocenter moves further away
220 from the station to accommodate this. The time-residuals for stations in other locations will evolve in
221 different ways. Over the next 9000 iterations, the D25K-P time-residual continues to decrease but
222 flattens off to a value of around -2.8 seconds. Note that the spread of time-residual estimates for
223 different trial hypocenters and origin times does not appear to decrease further. Similarly, the cloud
224 of trial hypocenters for the later iterations (the red dots in Figure 4a) cover an elliptical region about
225 4 by 7 km, elongated in a direction with a NNE strike. The size of this ellipse, together with the spread
226 in the time-residuals, provide a visual uncertainty estimate for the event displayed.

227 Figure 4b) displays the time-residual for the one event for every single trial hypocenter and origin
228 time. The most typically used parameters from Bayesloc output are the mean values for latitude,
229 longitude, depth, and origin time (once the so-called burn-in phase, in which the location estimates
230 may be qualitatively different to the end solutions, is removed). In Figure 5, we instead evaluate the
231 time-residual for mean hypocenter and origin time for each event for the six station-phase
232 combinations indicated. This plot indicates both the internal consistency within the aftershock zone
233 of the travel time residual for a given phase, and how the values vary from station to station. We see
234 in Figure 5e) that the large negative time residual we converge towards in Figure 4b) is typical for
235 almost all events in the cluster and would confirm the hypothesis of fast crust to the southwest of
236 the aftershock zone. The consistency of this residual term over the full population of events, covering
237 many months, essentially eliminates the hypothesis of a timing error on the station. The variability of
238 S-wave travel time residuals is generally somewhat higher than for P-wave travel time residuals. This
239 is likely related to the increased difficulty in picking the arrival time for the secondary phases.

240 The output from Bayesloc provides uncertainty statistics for the hypocenter distributions both
241 laterally and in depth. The median over Kaktovik events of the standard deviation for location in the
242 East-West direction was 4.2 km, while the median standard deviation in the North-South direction
243 was 6.2 km. This is consistent with the distribution of trial hypocenters displayed for the event in
244 Figure 4 and is a function of the network geometry. The median standard deviation in the depth was
245 3.8 km and the median standard deviation in the origin time was 0.65 seconds. The travel time from
246 hypocenter to station has a trade-off with depth and the travel time residuals, as displayed in Figure
247 5, are relatively insensitive to depth.

248 We focus here on the three closest stations to the aftershock zone to give maximum insight into the
249 northeasterly shift of the hypocenters. The Bayesloc solutions include all arrivals used in the AEC
250 catalog and therefore many hundreds of stations at far larger distances; the time-residuals further
251 from the source will be discussed later. The parallel calculation using a different baseline 1D velocity
252 model is a valuable check on robustness of the hypocenters. We increase the confidence in the
253 spatial distribution of hypocenters obtained if essentially the same distribution is obtained using a
254 somewhat different set of travel time tables; if the solution is robust, the solutions obtained from the
255 different baseline models should differ primarily only in the correction terms to travel time
256 predictions. We note also that only stations within regional distances are used in the AEC bulletin.
257 Given the magnitude distribution of the Kaktovik events (Ruppert and West, 2020) there are many
258 aftershocks that will be well recorded with good global coverage at teleseismic distances. Teleseismic
259 travel times are less susceptible to crustal heterogeneity (e.g. Myers et al., 2015) and augmenting the
260 bulletin with high quality teleseismic phases, with a wide azimuthal distribution, for the largest
261 events may provide additional constraints and reduce the sensitivity of the hypocenters to local
262 geologic heterogeneity.

263

264 **THE 2018/2019 EASTERN BROOKS RANGE EARTHQUAKE SWARM**

265 To the southwest of the aftershock zone considered in the previous sections is a distinct earthquake
266 swarm, referred to by Gaudreau et al. (2019) as the Niviak cluster. Ruppert and West (2020) describe
267 the temporal and magnitude distributions of both sequences; the Niviak cluster consists only of
268 events below magnitude 4.5 but is more enigmatic given the spatial distribution, the long duration,
269 and the absence of a causative mainshock. The swarm intensified in July 2018 (shortly prior to the
270 large Kaktovik earthquakes and their aftershocks), reached a peak in October 2018, before
271 decreasing over the fall of 2018. A new intensification of seismicity started in July/August 2019.

272 Figure 6a) displays the locations of the events throughout 2018 and 2019 from the AEC bulletin. We
273 have better azimuthal coverage for recording this swarm than for the Kaktovik earthquakes, with
274 multiple stations observing the sequence in all directions. This is especially true to the north where
275 the Kaktovik sequence relied on a single station, C26K. Bayesloc was run using the same arrivals as
276 were used to compile the AEC catalog; the results are displayed in Figure 6b). The large-scale
277 features are unchanged although many features can be identified which appear better resolved or
278 more cleanly separated in the multiple event location estimates. The most south easterly cluster at
279 68.55°N , -145.5°E becomes significantly more compact in the relocations. A double cluster in the AEC
280 network solutions at 68.8°N , -148.2°E resolves into two distinct clusters elongated in the direction of
281 the topographic features. The cluster at 69.2°N , -147.5°E migrates a few kilometers to the northwest
282 and appears to split into two; the change is easier to identify in Figure 6c) where the relocated event
283 positions are superimposed on top of the network solutions. The spatial separation between each of
284 the clusters in the northeast is a little more pronounced in the relocations than in the AEC catalog.

285 Given the fine structures and complex cluster patterns visible in the relocations, there is motivation
286 to perform full-waveform cluster analysis using cross-correlation or other signal semblance analysis.
287 A given arrival measurement can contribute to a location error in two ways: error in travel time
288 prediction and error in the arrival time measurement. Bayesloc mitigates the first of these in a way

289 that event-by-event network solutions cannot, although we are still only using analyst arrival picks in
290 this study and are still vulnerable to the uncertainty in the human-estimated arrival times. Using
291 relative time-delay measurements and double-difference location methods (e.g. Shearer, 1997;
292 Waldhauser and Ellsworth, 2000) may reveal geometrical structure at finer spatial scales not
293 resolvable using only absolute arrival time estimates; such a study is however beyond the scope of
294 this paper. Given that the maximum event magnitude is below 4.5, we are unlikely to be able to
295 exploit teleseismic data to improve location accuracy.

296

297 **DISCUSSION AND FUTURE PERSPECTIVES**

298 We have applied the probabilistic multiple event location algorithm Bayesloc to two seismic
299 sequences in northern Alaska for which most of the phase arrivals were provided by stations of the
300 EarthScope USArray Transportable Array. In the first, aftershocks of the 12 August 2018 Kaktovik
301 earthquakes, Bayesloc made a small but significant relocation of the entire cluster. The relocated
302 event cluster has a far sharper southernmost boundary with a strike angle consistent with non-
303 seismological constraints on the fault plane. In the second, the Niviak cluster, the probabilistic event
304 locations are significantly more clustered and indicate clearer separation between localized zones of
305 seismicity. Without the TA stations, we would not have the detection threshold or the station
306 coverage to be able to resolve these sequences.

307 Full-waveform cluster analysis, using correlation methods to measure both signal similarity and
308 enhanced time-delay estimates, is likely to provide improved local scale resolution of the seismicity
309 in both sequences. The feature of Bayesloc which appears to be most powerful in these cases is the
310 ability to solve for corrections to travel time predictions for given paths. The exploitation of readings
311 from multiple events to account for, or to eliminate, bias in travel time estimates is a cornerstone of
312 many advanced seismic event location algorithms (e.g. Douglas, 1967; Richards-Dinger and Shearer,
313 2000; Nooshiri et al., 2017). The solutions obtained using Bayesloc indicate that failure to account for

314 anomalously fast propagation to the southwest of the Kaktovik aftershock is the primary reason that
315 the network locations in many cases lie to the south of the InSAR-inferred fault line.

316 In Figure 5 we display spatially consistent time-residuals for P- and S- phases at the three stations
317 closest to the Kaktovik aftershocks. In Figure 7, instead of a single travel time residual per event for a
318 given phase, we display the median travel-time residual for all events in the Kaktovik sequence for P-
319 and S- arrivals at each station. The blue symbols to the southwest of the earthquakes (the yellow
320 square) are of similar colors to the symbols in panels e) and f) of Figure 5 and indicate the faster
321 propagation along these paths. It should be noted that the geological heterogeneity over this short
322 path is not necessarily more extreme than elsewhere in Alaska. The waves arriving at more distant
323 stations from the Kaktovik earthquakes have travelled longer paths over which the contribution to
324 the travel time from regions with anomalously fast propagation will cancel with the contributions
325 from regions with anomalously slow propagation.

326 The travel time residuals displayed in Figure 7 are relative to one specific 1-dimensional velocity
327 model. However, the location calculations were repeated using alternative velocity models and we
328 confirm that the large-scale features of the relocated clusters of seismicity are largely unchanged.
329 The travel time residual plots for AK135 (corresponding to Figures 5 and 7) look somewhat different
330 as different corrections are required to compensate for the deficiencies of the baseline model along
331 the different paths. Relative insensitivity to the details of the underlying 1-D model was also
332 demonstrated by Gibbons et al. (2017). Another feature of Figure 7 that increases our confidence
333 that the residuals are related to 3-dimensional geologic properties and not a simple inapplicability of
334 the underlying 1D model is the distribution of high positive P-wave time-residuals for stations to the
335 south of the map. The size of the residuals does not increase simply with distance from the source;
336 the highest residuals are found to the South of the Chugach Mountains and indicate slow
337 propagation along these specific paths.

338 Repeating the procedure applied here to clusters of seismicity across Alaska would generate
339 corresponding maps which could be used to validate existing 3-dimensional tomographic images and
340 provide input for large scale evaluations of 3-d velocity maps. Similar studies have been performed
341 both globally and regionally (e.g. Myers et al., 2011, and Simmons et al., 2012) and applying such a
342 procedure to Alaska now would benefit from the recently improved station coverage. There is no
343 limit, in principle, as to how large the datasets for the Bayesloc program can be. In practice, the
344 computational cost of calculating the joint probability distributions increases greatly with the number
345 of events and phases; the 40000-iteration calculation for the Kaktovik aftershock sequence with 4192
346 events and 109905 phases took approximately 11.5 hours on a high-end Linux workstation. Simply
347 covering all historical seismicity over all of Alaska and adding new events with all readings as they
348 occur is not a viable strategy for near real-time event location with current technology. Bayesloc,
349 however, can take prior information regarding both uncertainty in event hypocenters and origin
350 times and travel time predictions; results from previous runs can be used to constrain subsequent
351 runs without needing to include all the raw inputs. Whereas only a subset of Alaska TA stations will
352 be transitioned into longer-term operation, the contribution of any of the TA stations that are
353 removed will always be valuable in the framework of probabilistic multiple event location algorithms.

354 **ACKNOWLEDGEMENTS**

355 This research was supported in part by the Geophysical Institute – University of Alaska Fairbanks and
356 Office of Alaska State Seismologist (N.A.R., E.K.).

357 The facilities of IRIS Data Services, and specifically the IRIS Data Management Center, were used for
358 access to waveforms, related metadata, and/or derived products used in this study. IRIS Data
359 Services are funded through the Seismological Facilities for the Advancement of Geoscience (SAGE)
360 Award of the National Science Foundation under Cooperative Service Agreement EAR-1851048.

361 Data from the TA network (IRIS Transportable Array, 2003) were made freely available as part of the
362 EarthScope USArray facility, operated by Incorporated Research Institutions for Seismology (IRIS) and
363 supported by the National Science Foundation, under Cooperative Agreements EAR-1261681.

364 We are very grateful to Geoffrey Abers, Steve Myers, and an anonymous reviewer for very
365 constructive comments and suggestions which led to a significant improvement in this paper.

366

367 **DATA AND RESOURCES**

368 All maps generated by the GMT package, Wessel and Smith (1995) (Generic Mapping Tool:
369 <https://www.soest.hawaii.edu/gmt/>). (last accessed June 6, 2020)

370 Original earthquake hypocenters and phase picks are from the Alaska Earthquake Center Catalog.

371 Earthquake relocations were performed using the Bayesloc program, available for download from
372 <https://www-gs.llnl.gov/nuclear-threat-reduction/nuclear-explosion-monitoring/bayesloc>

373 (last accessed June 6, 2020).

374 The website of the EarthScope USArray is www.usarray.org (last accessed June 6, 2020)

375

376

377 **REFERENCES**

- 378 Busby, R. W. and Aderhold, K. (2020). The Alaska Transportable Array: As Built, *Seismological*
379 *Research Letters*, (in press, this issue)
- 380 Douglas, A. (1967), Joint Epicentre Determination, *Nature* 215, 47-48, [10.1038/215047a0](https://doi.org/10.1038/215047a0)
- 381 Estabrook, C., Stone, D. B. and Davies, J. N. (1988). Seismotectonics of northern Alaska, *Journal of*
382 *Geophysical Research*, V93 issue B10, 12026-12040,
383 <https://doi.org/10.1029/JB093iB10p12026>.
- 384 Fuis, G. S., Murphy, J. M., Lutter, W. J., Moore, T. E., Bird, K. J., & Christensen, N. I. (1997). Deep
385 seismic structure and tectonics of northern Alaska: Crustal-scale duplexing with deformation
386 extending into the upper mantle. *Journal of Geophysical Research: Solid Earth*, 102(B9),
387 20873–20896. <https://doi.org/10.1029/96jb03959>
- 388 Gaudreau, É., Nissen, E. K., Bergman, E. A., Benz, H. M., Tan, F., & Karasözen, E. (2019). The August
389 2018 Kaktovik Earthquakes: Active Tectonics in Northeastern Alaska Revealed With InSAR
390 and Seismology. *Geophysical Research Letters*, 2019GL085651.
391 <https://doi.org/10.1029/2019GL085651>
- 392 Gedney, L., N. Biswas, Huang, P., Estes, S., and Pearson, C. (1977). Seismicity of Northeast Alaska,
393 *Geophysical Research Letters*, V4, no. 5, pp. 175-177.
394 <https://doi.org/10.1029/GL004i005p00175>
- 395 Gibbons, S. J., and Kväerna, T. (2017). Illuminating the seismicity pattern of the October 8, 2005, M =
396 7.6 Kashmir earthquake aftershocks. *Physics of the Earth and Planetary Interiors*, 270, 1–8.
397 <https://doi.org/10.1016/j.pepi.2017.06.008>
- 398 Gibbons, S J, Harris, D. B., Dahl-Jensen, T., Kväerna, T., Larsen, T. B., Paulsen, B., & Voss, P. H. (2017).
399 Locating seismicity on the Arctic plate boundary using multiple-event techniques and

- 400 empirical signal processing. *Geophysical Journal International*, 211(3), 1613–1627.
401 <https://doi.org/10.1093/GJI/GGX398>
- 402 Hayes, G. P., Briggs, R. W., Barnhart, W. D., Yeck, W. L., McNamara, D. E., Wald, D. J., Nealy, J L., Benz,
403 H. M., Gold, R. D., Jaiswal, K. S., Marano, K., Earle, P. S., Hearne, M. G., Smoczyk, G. M., Wald,
404 L. A., & Samsonov, S. V. (2015). Rapid Characterization of the 2015 Mw 7.8 Gorkha, Nepal,
405 Earthquake Sequence and Its Seismotectonic Context. *Seismological Research Letters*, 86(6),
406 1557–1567. <https://doi.org/10.1785/0220150145>
- 407 IRIS Transportable Array (2003). USArray Transportable Array. International Federation of Digital
408 Seismograph Networks, Dataset/Seismic Network, <https://doi.org/10.7914/SN/TA>
- 409 Kennett, B. L. N., Engdahl, E. R., and R. Buland (1995). Constraints on seismic velocities in the Earth
410 from travel times, *Geophysical Journal International* **122**, 108-124. [10.1111/j.1365-](https://doi.org/10.1111/j.1365-246x.1995.tb03540.x)
411 [246x.1995.tb03540.x](https://doi.org/10.1111/j.1365-246x.1995.tb03540.x)
- 412 Koehler, R. D., Farrell, R.-E., Burns, P. A. C. and Combellick, R. A. (2012). Quaternary faults and folds in
413 Alaska: A digital database, 31p., 1 sheet, 1:3,700,000, Alaska Division of Geological &
414 Geophysical Surveys Digital Data Series 3. Fairbanks, Alaska, USA.
415 <http://dx.doi.org/10.14509/23944>
- 416 Leonard, L. J., Mazzotti, S. and Hyndman, R. D. (2008). Deformation rates from earthquakes in the
417 northern Cordillera of Canada and eastern Alaska, *Journal of Geophysical Research*, 113,
418 B08406, [doi:10.1029/2007JB005456](https://doi.org/10.1029/2007JB005456)
- 419 Mazzotti, S., and Hyndman, R. D. (2002), Yakutat collision and strain transfer across the northern
420 Canadian Cordillera. *Geology*, 30, 495-498, 2002. [https://doi.org/10.1130/0091-](https://doi.org/10.1130/0091-7613(2002)030<0495:YCASTA>2.0.CO;2)
421 [7613\(2002\)030<0495:YCASTA>2.0.CO;2](https://doi.org/10.1130/0091-7613(2002)030<0495:YCASTA>2.0.CO;2)

- 422 Mazzotti, S., Leonard, L. J., Hyndman, R. D., and Cassidy, J. F. (2008). Tectonics, Dynamics, and
423 Seismic Hazard in the Canada–Alaska Cordillera, *Active Tectonics and Seismic Potential of*
424 *Alaska*, AGU Geophysical Monograph Series, 179, <https://doi.org/10.1029/179GM17>
- 425 Myers, S. C., Johannesson, G., and Hanley, W. (2007), A Bayesian hierarchical method for multiple-
426 event seismic location, *Geophysical Journal International* 171, 1049-1063,
427 doi:10.1111/j.1365-246x.2007.03555.x
- 428 Myers, S. C., Johannesson, G., & Hanley, W. (2009). Incorporation of probabilistic seismic phase labels
429 into a Bayesian multiple-event seismic locator. *Geophysical Journal International*, 177(1),
430 193–204. <https://doi.org/10.1111/j.1365-246x.2008.04070.x>
- 431 Myers, S. C., Johannesson, G., and Simmons, N. A. (2011). Global-scale P wave tomography optimized
432 for prediction of teleseismic and regional travel times for Middle East events: 1. Data set
433 development. *Journal of Geophysical Research* 116, B04304+. [doi:10.1029/2010jb007967](https://doi.org/10.1029/2010jb007967)
- 434 Myers, S. C., Simmons, N. A., Johannesson, G., and Matzel, E. (2015). Improved Regional and
435 Teleseismic P-Wave Travel-Time Prediction and Event Location Using a Global 3D Velocity
436 Model. *Bulletin of the Seismological Society of America* 105, 1642–1660.
437 [doi:10.1785/0120140272](https://doi.org/10.1785/0120140272).
- 438 Nealy, J. L., Benz, H. M., Hayes, G. P., Bergman, E. A., & Barnhart, W. D. (2017). The 2008 Wells,
439 Nevada, Earthquake Sequence: Source Constraints Using Calibrated Multiple-Event
440 Relocation and InSAR. *Bulletin of the Seismological Society of America*, **107**, 1107-1117.
441 <https://doi.org/10.1785/0120160298>
- 442 Nooshiri, N., Saul, J., Heimann, S., Tilmann, F., and Dahm, T. (2017), Revision of earthquake
443 hypocentre locations in global bulletin data sets using source-specific station terms,
444 *Geophysical Journal International* **208**, 589-602, [doi:10.1093/gji/ggw405](https://doi.org/10.1093/gji/ggw405)

- 445 Pyle, M. L., Myers, S. C., Walter, W. R., & Smith, K. D. (2015). Accurate Local Event Locations in Rock
446 Valley, Nevada, Using a Bayesian Multiple-Event Method. *Bulletin of the Seismological Society*
447 *of America*, **105**, 706-718. <https://doi.org/10.1785/0120140251>
- 448 Richards-Dinger, K. B., and Shearer, P. M. (2000), Earthquake locations in southern California
449 obtained using source-specific station terms, *Journal of Geophysical Research* **105**, 10939-
450 10960, [doi:10.1029/2000jb900014](https://doi.org/10.1029/2000jb900014)
- 451 Ruppert, N. A., & West, M. E. (2020). The Impact of USArray on Earthquake Monitoring in Alaska.
452 *Seismological Research Letters*, 91(2A), 601-610. <https://doi.org/10.1785/0220190227>
- 453 Shearer, P. M. (1997). Improving local earthquake locations using the L1 norm and waveform cross
454 correlation: Application to the Whittier Narrows, California, aftershock sequence, *Journal of*
455 *Geophysical Research* **102**, 8269-8283. [doi:10.1029/96jb03228](https://doi.org/10.1029/96jb03228)
- 456 Simmons, N. A., Myers, S. C., Johannesson, G., and Matzel, E. (2012). LLNL-G3Dv3: Global P wave
457 tomography model for improved regional and teleseismic travel time prediction. *Journal of*
458 *Geophysical Research* **117**, B10302+. [doi:10.1029/2012jb009525](https://doi.org/10.1029/2012jb009525)
- 459 Storchak, D. A., Schweitzer, J., & Bormann, P. (2003). The IASPEI Standard Seismic Phase List.
460 *Seismological Research Letters*, 74(6), 761–772.
- 461 Waldhauser, F. and Ellsworth, W. L. (2000), A Double-Difference Earthquake Location Algorithm:
462 Method and Application to the Northern Hayward Fault, California, *Bulletin of the*
463 *Seismological Society of America* **90**, 1353-1368. [doi:10.1785/0120000006](https://doi.org/10.1785/0120000006)
- 464 Wessel, P. and W. H. F. Smith (1995). New version of the generic mapping tools released, *EOS*
465 *Transactions, American Geophysical Union* **76**, no. 33, 329.

466 **Figure Captions**

467 **Figure 1 Subset of the earthquake catalog from the Alaska Earthquake Center (2017-2019)**
468 **including the aftershocks of the 12 August 2018 Kaktovik sequence and the 2018 Eastern Brooks**
469 **Range swarm together with the closest available stations. BMAR is the Burnt Mountain seismic**
470 **array, consisting of 5 short-period vertical component seismometers within an aperture of**
471 **approximately 5 km. The M_w 6.0 and M_w 6.4 earthquakes on 12 August 2018 are marked with five**
472 **and six-sided polygons respectively.**

473
474 **Figure 2 All events in the catalog of the Alaska Earthquake Center for the region displayed in the**
475 **time period 2018-2019 (a) as reported in the AEC catalog, (b) as relocated by Bayesloc using only**
476 **the arrival picks from the AEC catalog, and (c) with the relocated hypocenters plotted over the**
477 **catalog hypocenters with the same color scales. The symbols in (d) are drawn at the locations of**
478 **the relocated hypocenters with a color indicating the direction from the relocated epicenter to the**
479 **catalog epicenter. The blue colors indicate that the catalog locations for almost all events lie to the**
480 **southwest of the relocated events. The M_w 6.0 and M_w 6.4 earthquakes on 12 August 2018 are**
481 **marked with five and six-sided polygons respectively. In panel c) the catalog location of the M_w 6.0**
482 **earthquake is marked with a black pentagon outline. The white lines in panels a), b) and c) indicate**
483 **the surface projections of the InSAR-modelled buried fault segments from Gaudreau et al. (2019).**

484
485 **Figure 3 Relocation vectors for all events displayed in Figure 2. We define the catalog location of**
486 **each event to be at the origin and plot the relocated hypocenter relative to the catalog**
487 **hypocenter. Size of the symbol is proportional to the event magnitude. The M_w 6.0 and M_w 6.4**
488 **earthquakes on 12 August 2018 are marked with five and six-sided polygons respectively.**

489

490 **Figure 4 Evolution of the location estimate for a single earthquake in the sequence as a function of**
491 **iteration number in the Monte Carlo Markov Chains of the Bayesloc program. The white symbols in**
492 **panel (a) display the mean epicenters for all events in the sequence and the small colored symbols**
493 **indicate the epicenter location for event 6155 colored according to the iteration. Panel (b) displays**
494 **the observed minus predicted travel time residual with respect to the 1D velocity model for the**
495 **first P-arrival at station D25K. The M_w 6.0 and M_w 6.4 earthquakes on 12 August 2018 are marked**
496 **with five and six-sided polygons respectively.**

497
498 **Figure 5 Observed minus predicted travel time residuals for relocated events in the Kaktovik**
499 **sequence for C26K P-phase (a), C26K S (b), C27K P (c), C27K S (d), D25K P (e), and D25K S (f) relative**
500 **to the 1D velocity model used to locate the events. The M_w 6.0 and M_w 6.4 earthquakes on 12**
501 **August 2018 are marked with five and six-sided polygons respectively.**

502
503 **Figure 6 Locations of earthquakes in the Eastern Brooks Range swarm (a) from the catalog of the**
504 **Alaska Earthquake Center, (b) from the Bayesloc relocations, and (c) with the two sets of**
505 **hypocenters superimposed with the same color code.**

506
507 **Figure 7 Median observed minus predicted travel time residuals for first P (a) and first S (b) arrivals**
508 **from events in the Kaktovik aftershock sequence given the hypocenters and origin times from the**
509 **Bayesloc relocation. Blue symbols indicate an earlier than predicted arrival and red symbols**
510 **indicate a later than predicted arrival. The yellow square indicates the location of the largest**
511 **earthquake on 12 August 2018. A symbol indicates that the phase and station combination**
512 **appeared in the catalog of the Alaska Earthquake Center for at least 25 events in the sequence.**

513

514 Steven J. Gibbons, NGI, Sognsveien 72, 0855 Oslo, Norway. steven.gibbons@ngi.no +47 98613288

515 (corresponding author)

516 Natalia A. Ruppert, Alaska Earthquake Center, Geophysical Institute, University of Alaska Fairbanks,

517 2156 Koyukuk Drive, Fairbanks, Alaska 99775 U.S.A.

518 Ezgi Karasözen, Alaska Earthquake Center, Geophysical Institute, University of Alaska Fairbanks, 2156

519 Koyukuk Drive, Fairbanks, Alaska 99775 U.S.A.

520 Kasey Aderhold, IRIS, 1200 New York Avenue NW, Suite 400, Washington, D.C., 20005, U.S.A.

521 Ian Dickson, 310 West Archer Pl. #302, Denver, CO 80223. (formerly at the Alaska Earthquake Center,

522 Geophysical Institute, University of Alaska Fairbanks, 2156 Koyukuk Drive, Fairbanks, Alaska 99775

523 U.S.A.)

524

Figure 1

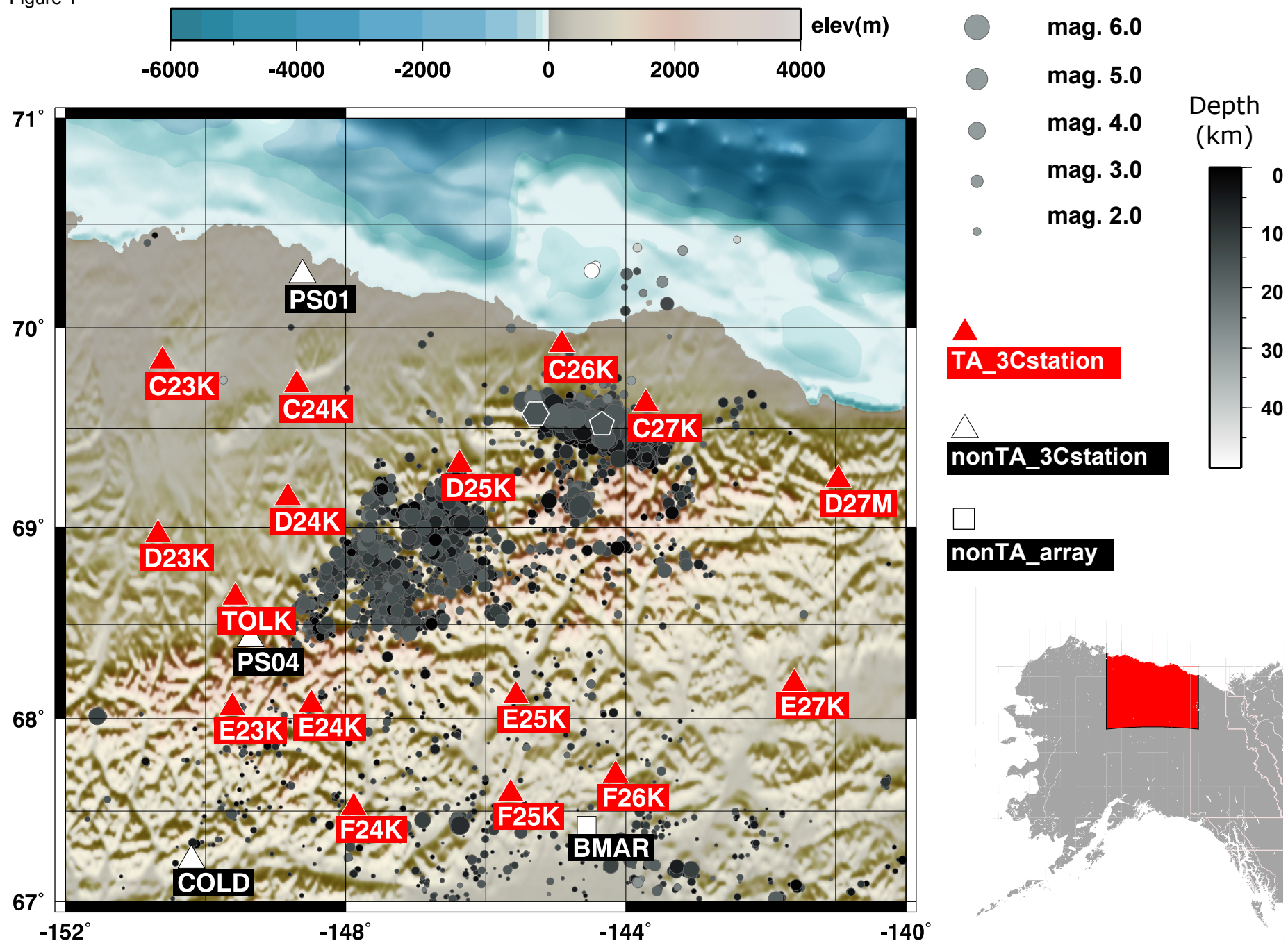


Figure 2

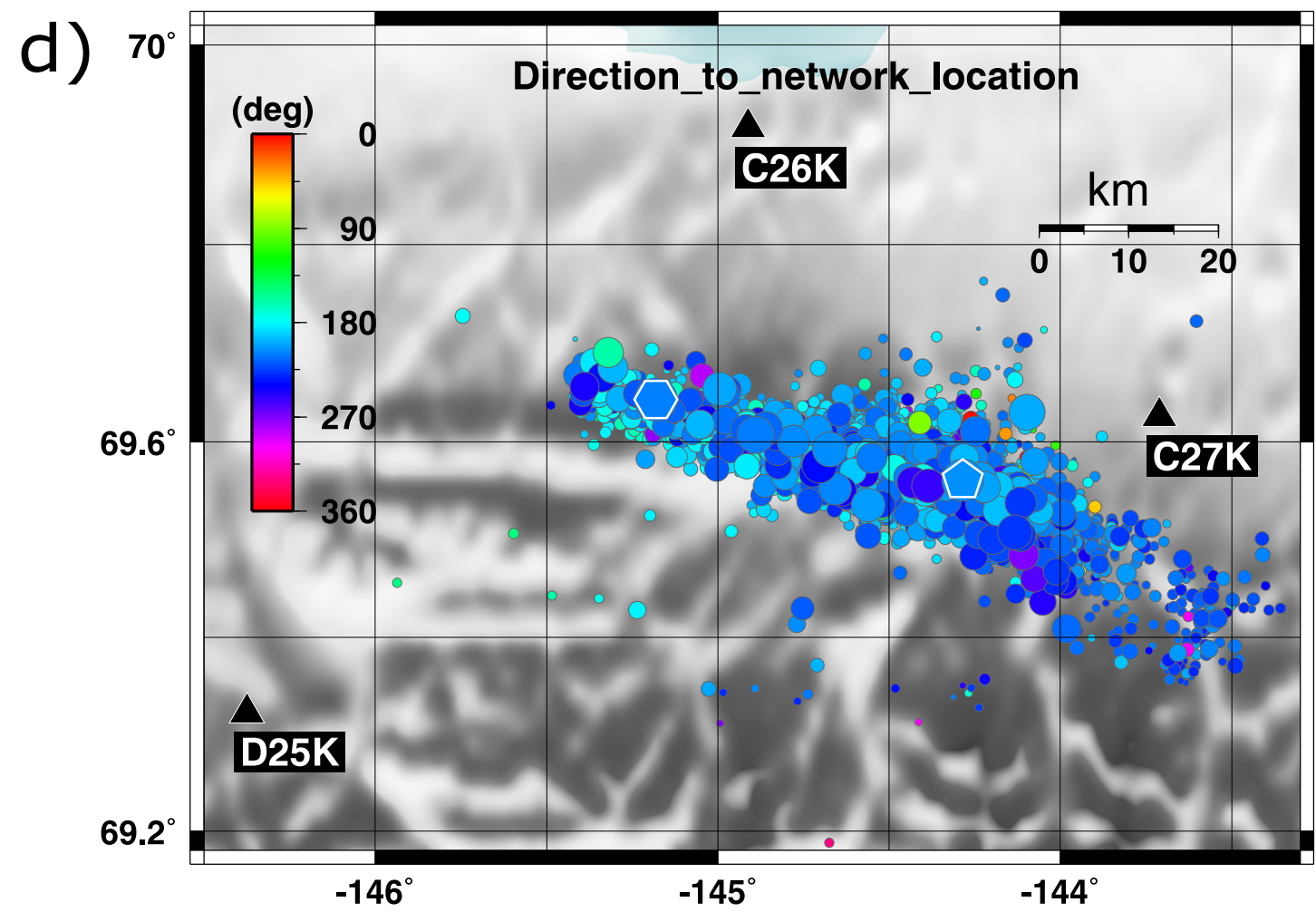
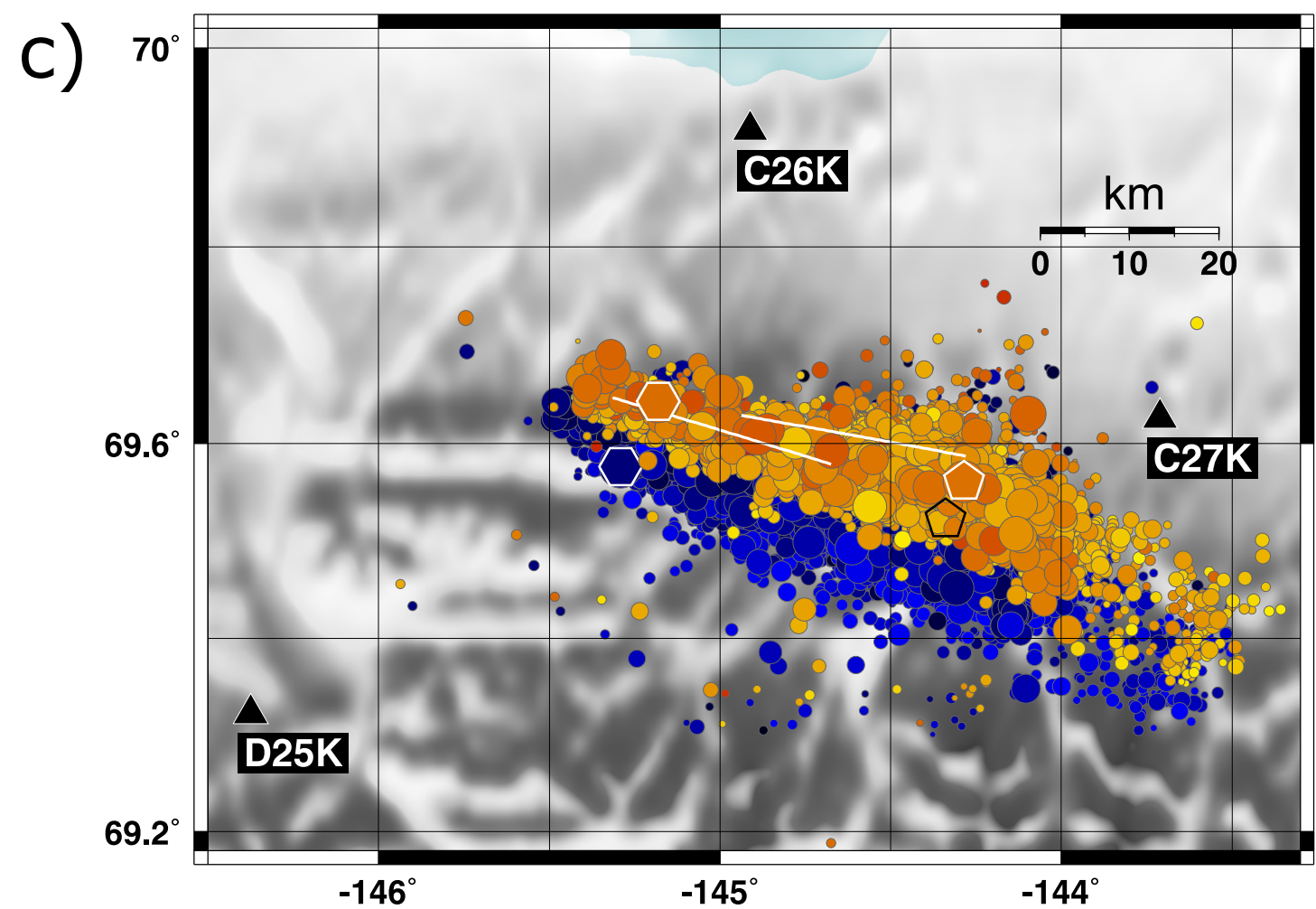
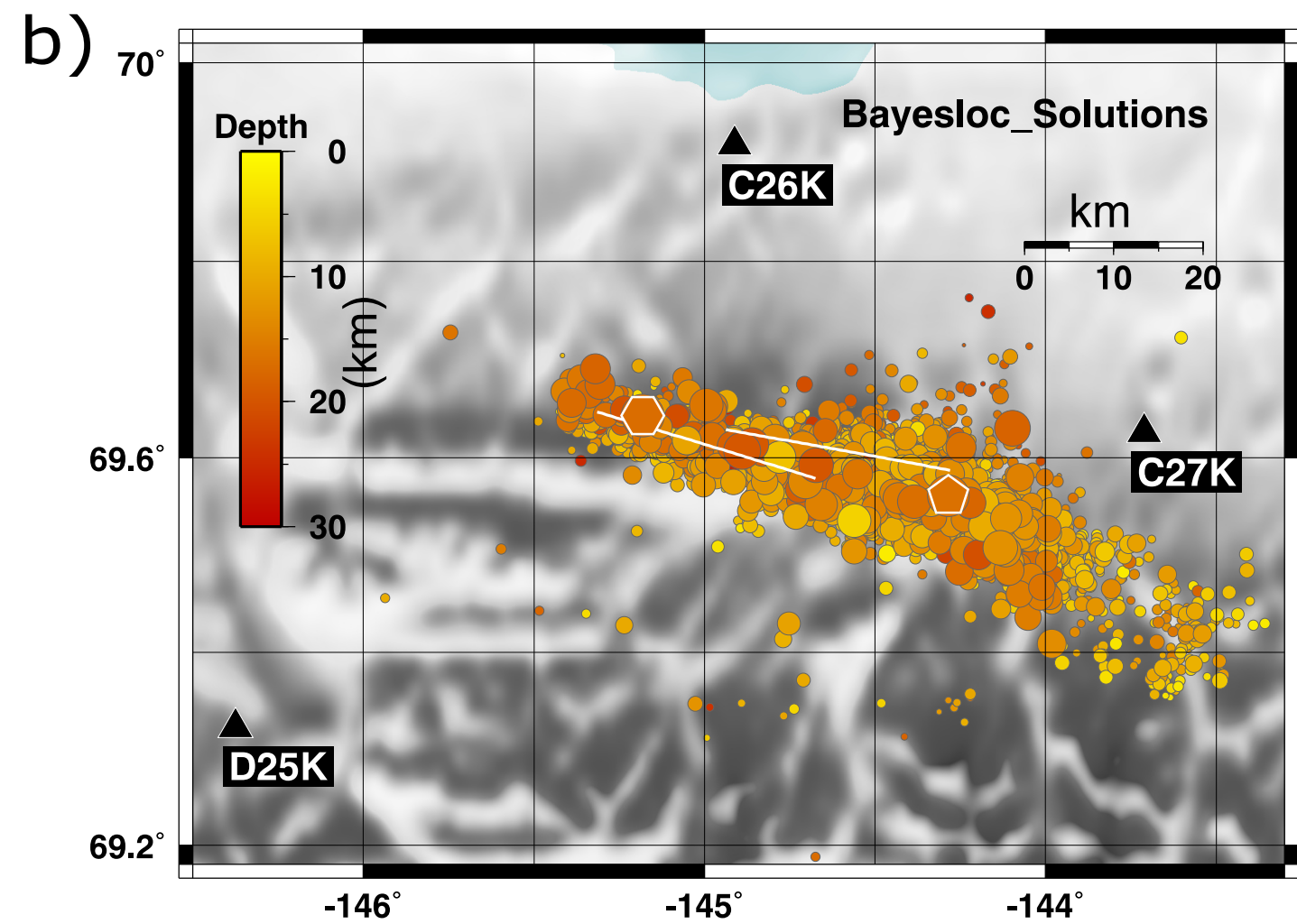
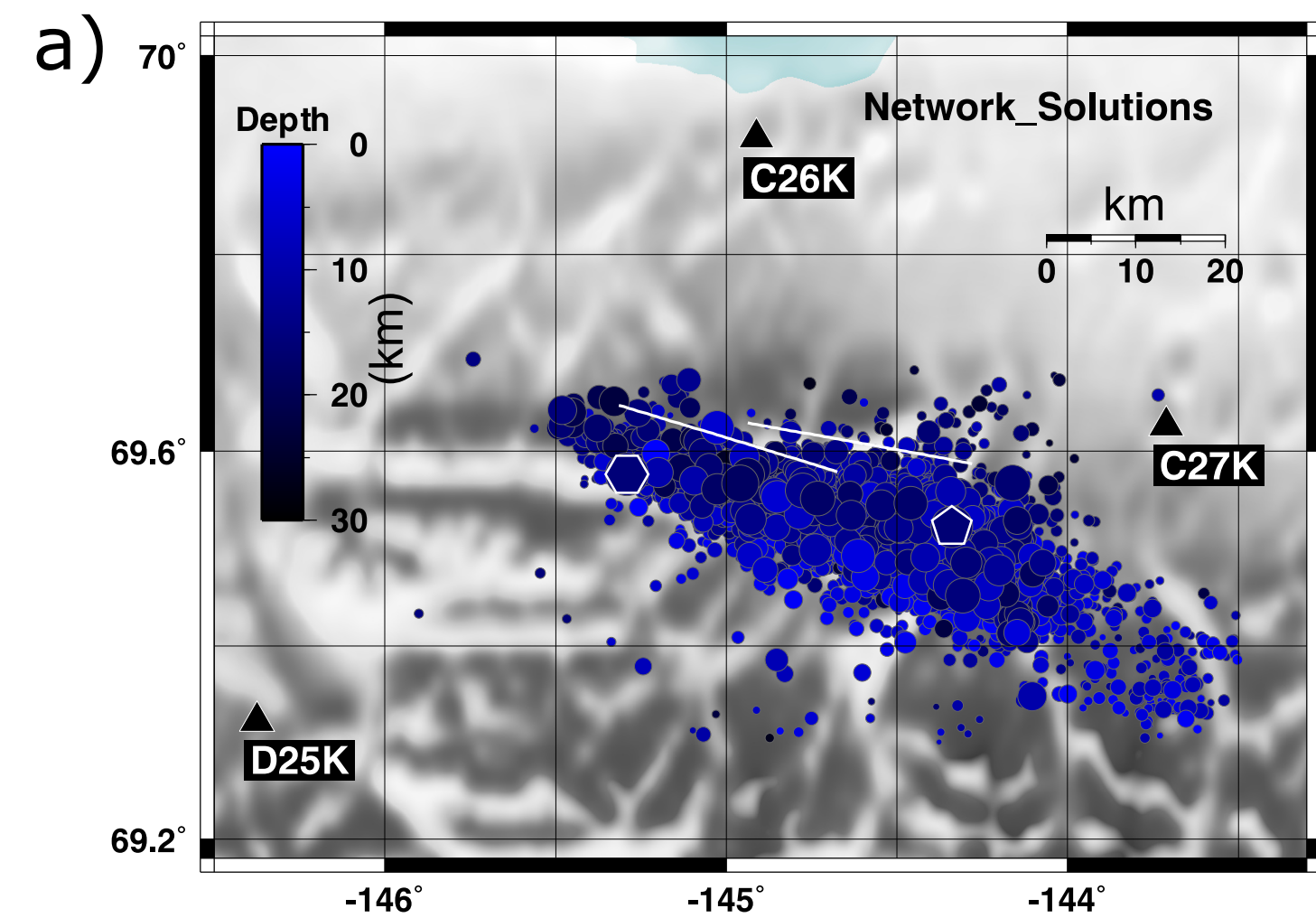
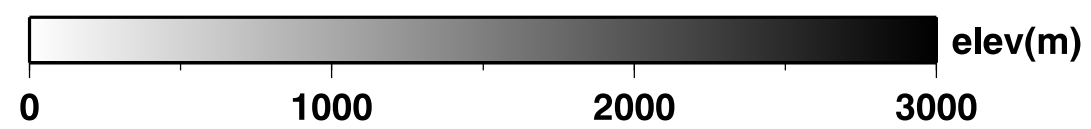


Figure 3

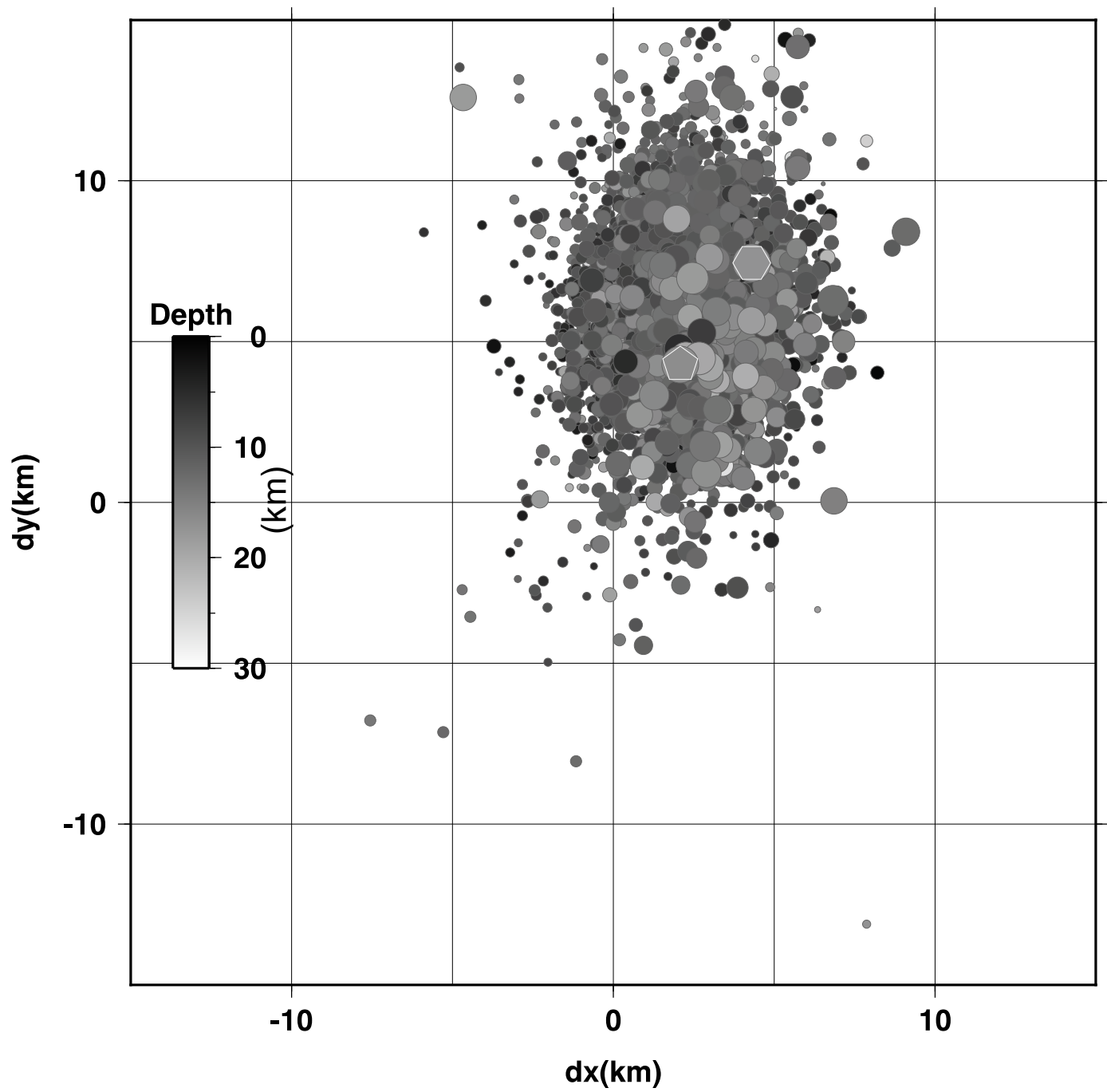
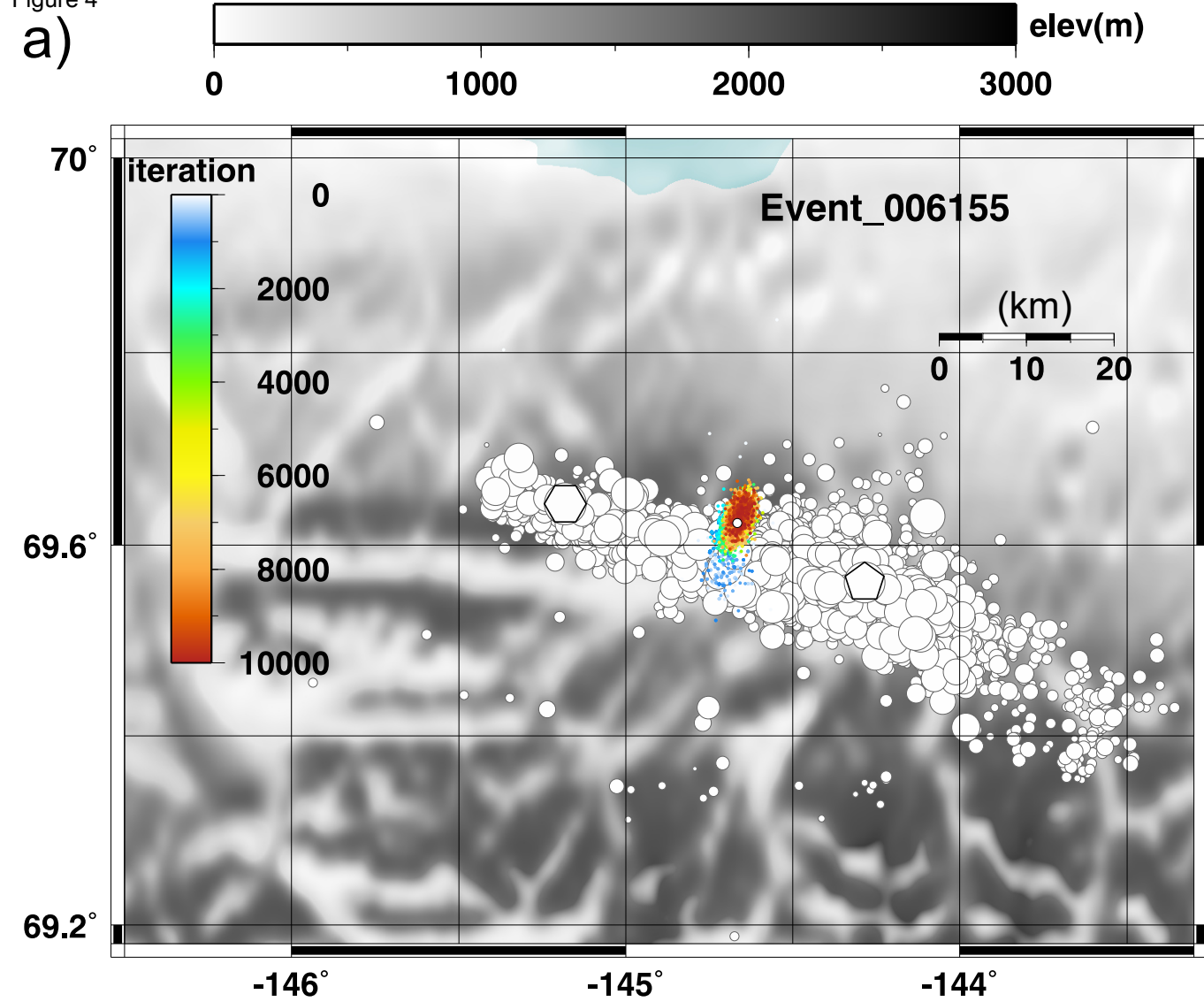
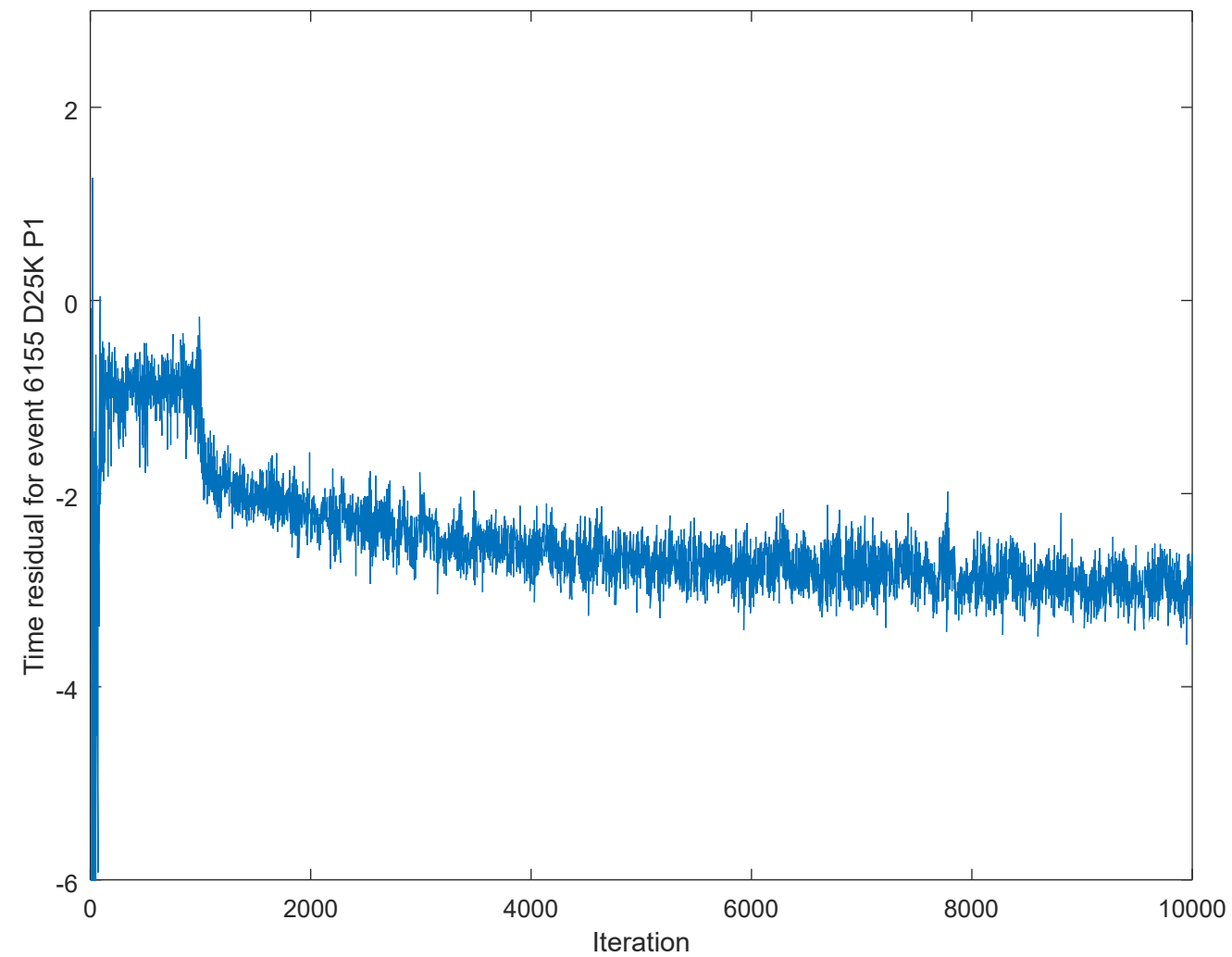


Figure 4



b)



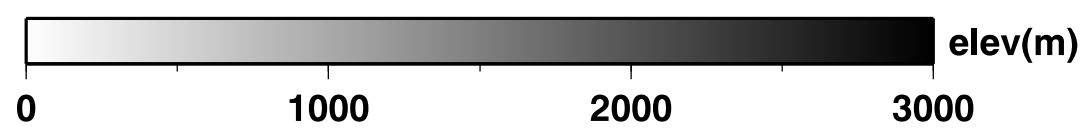
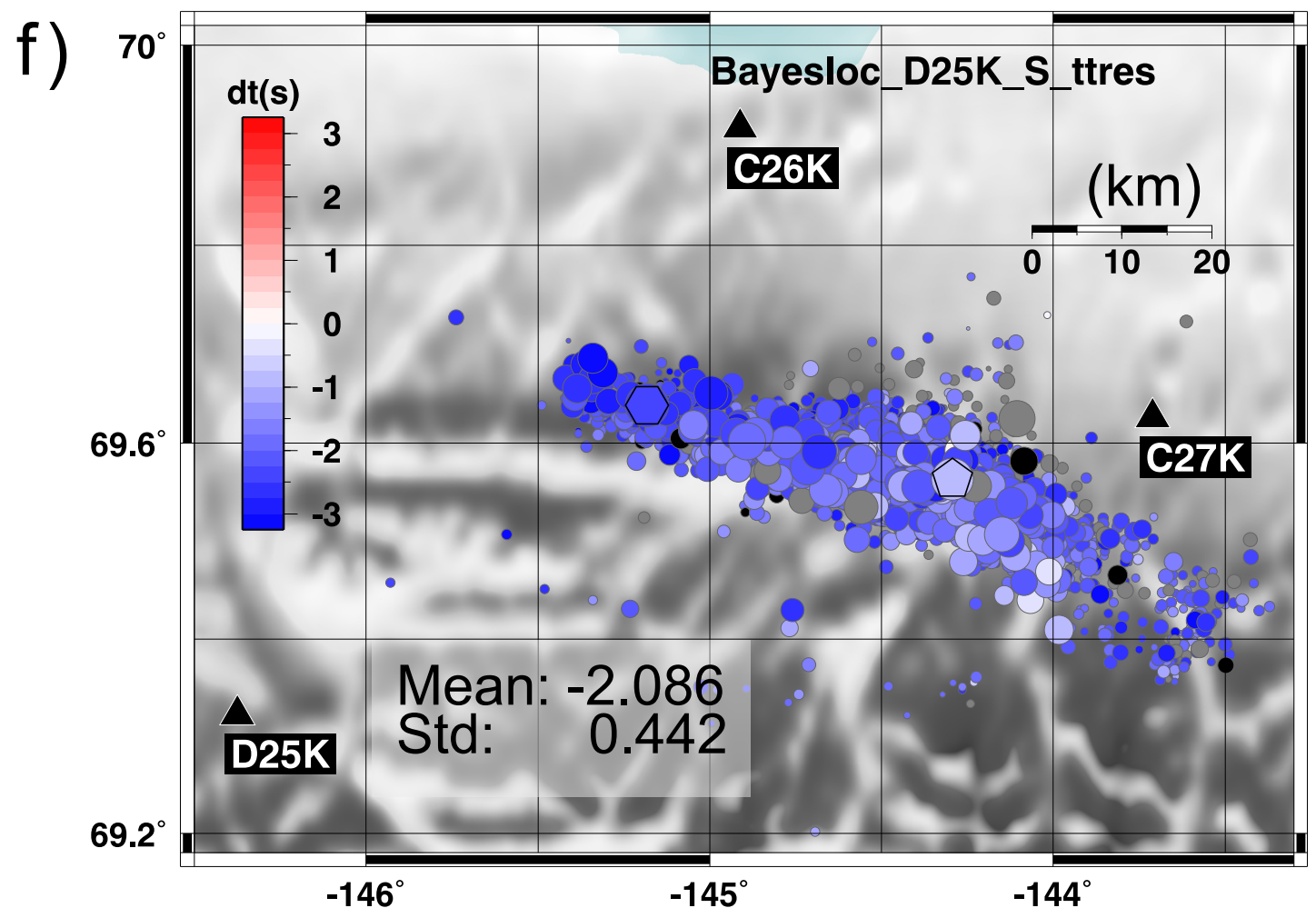
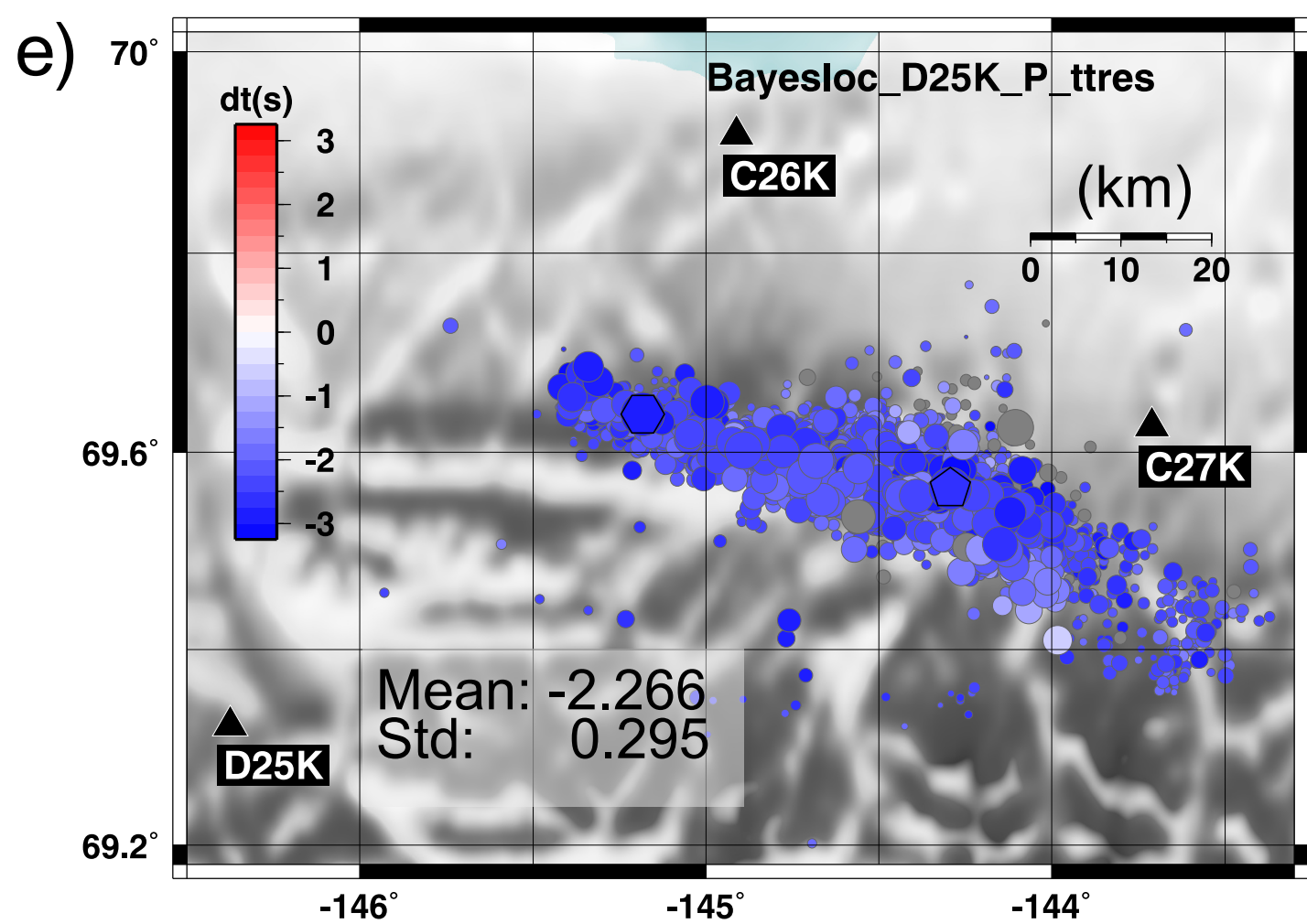
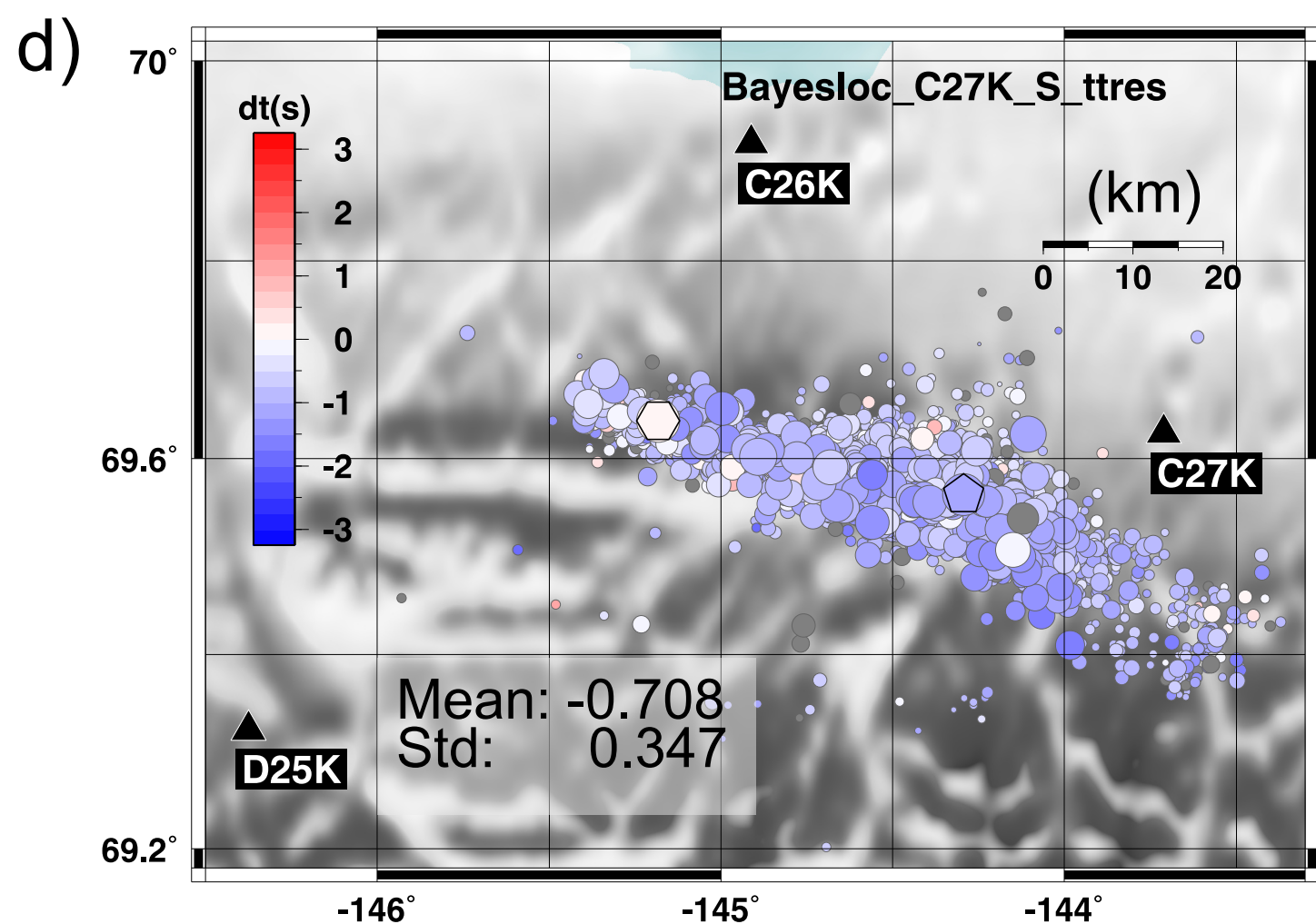
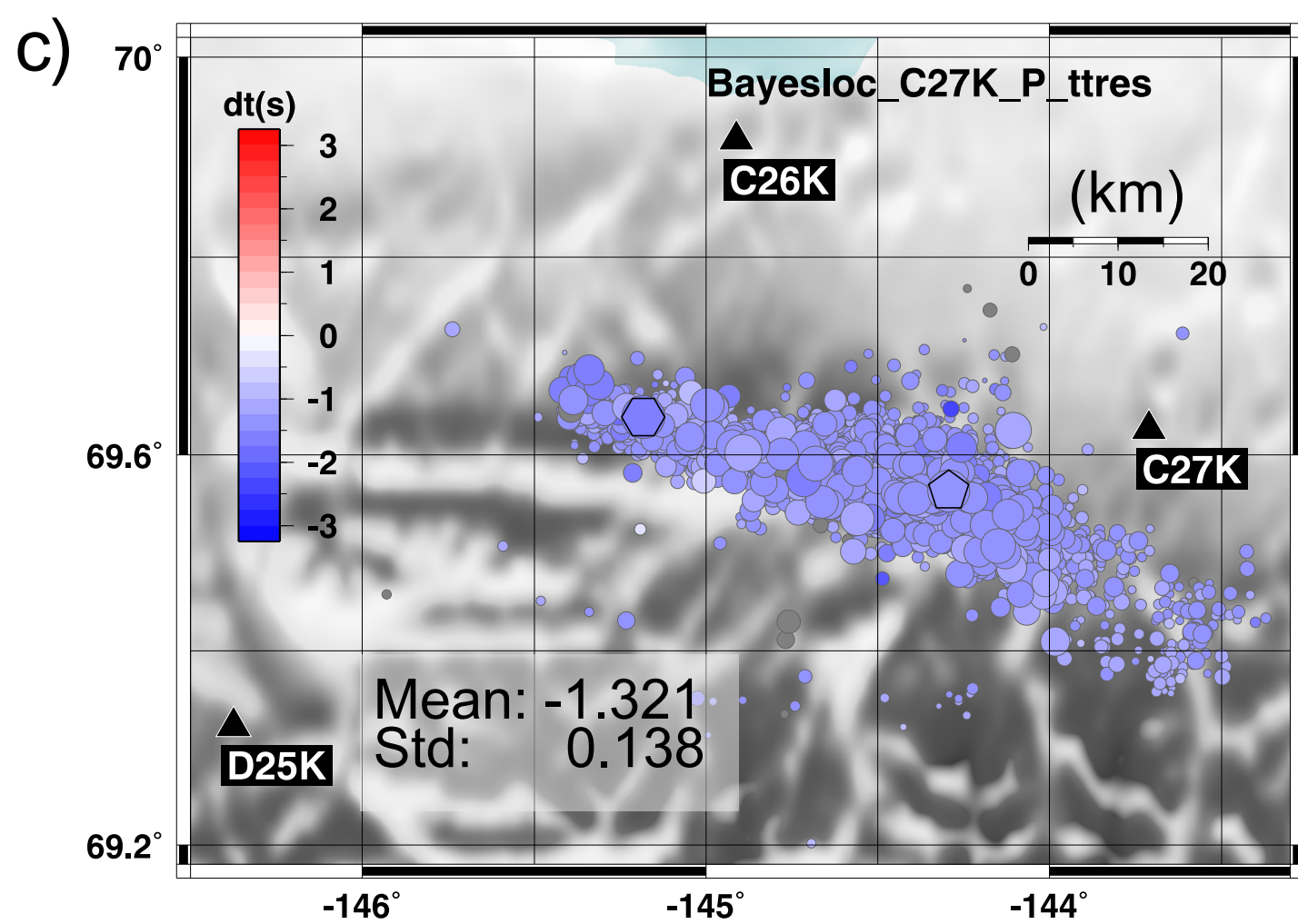
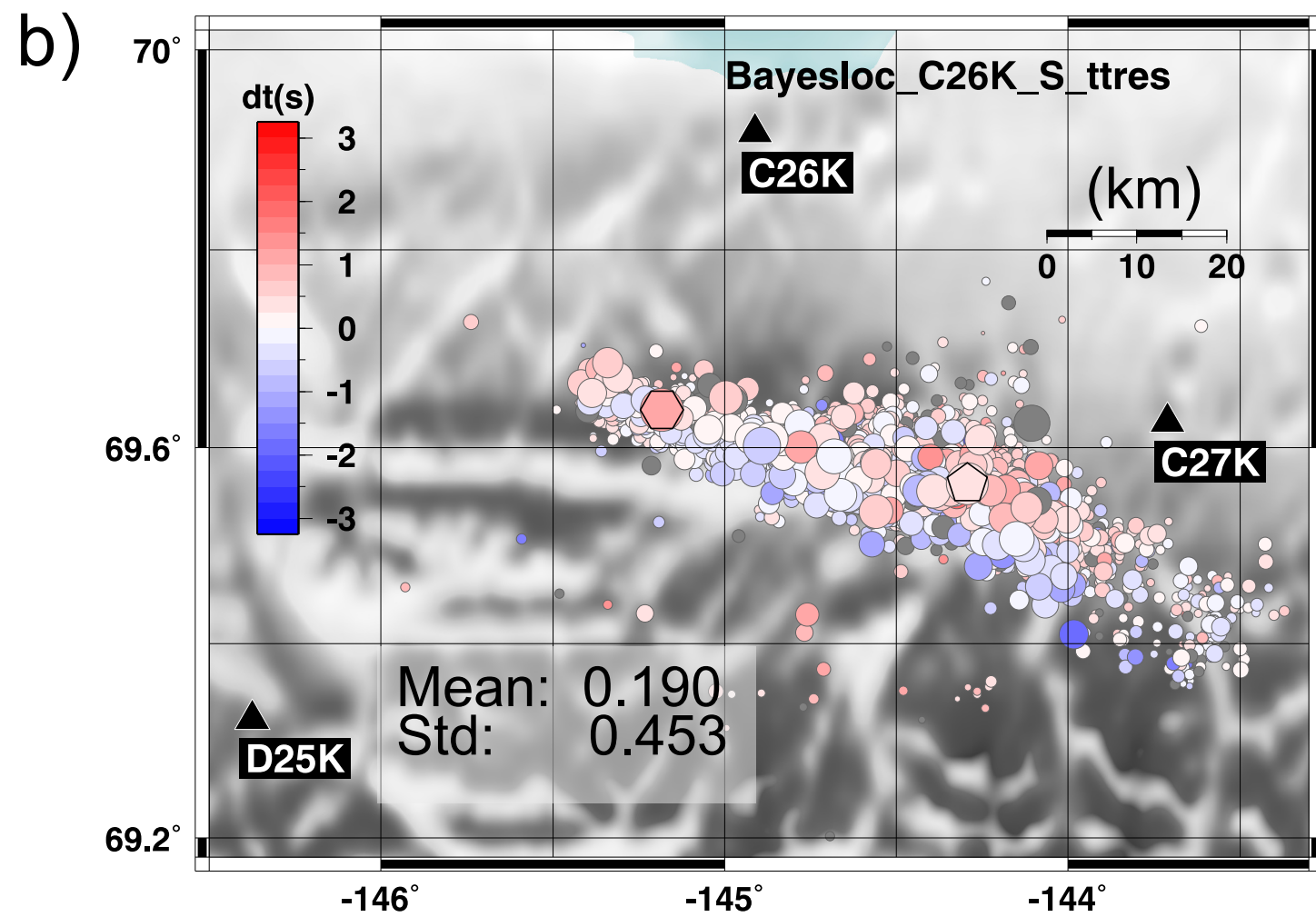
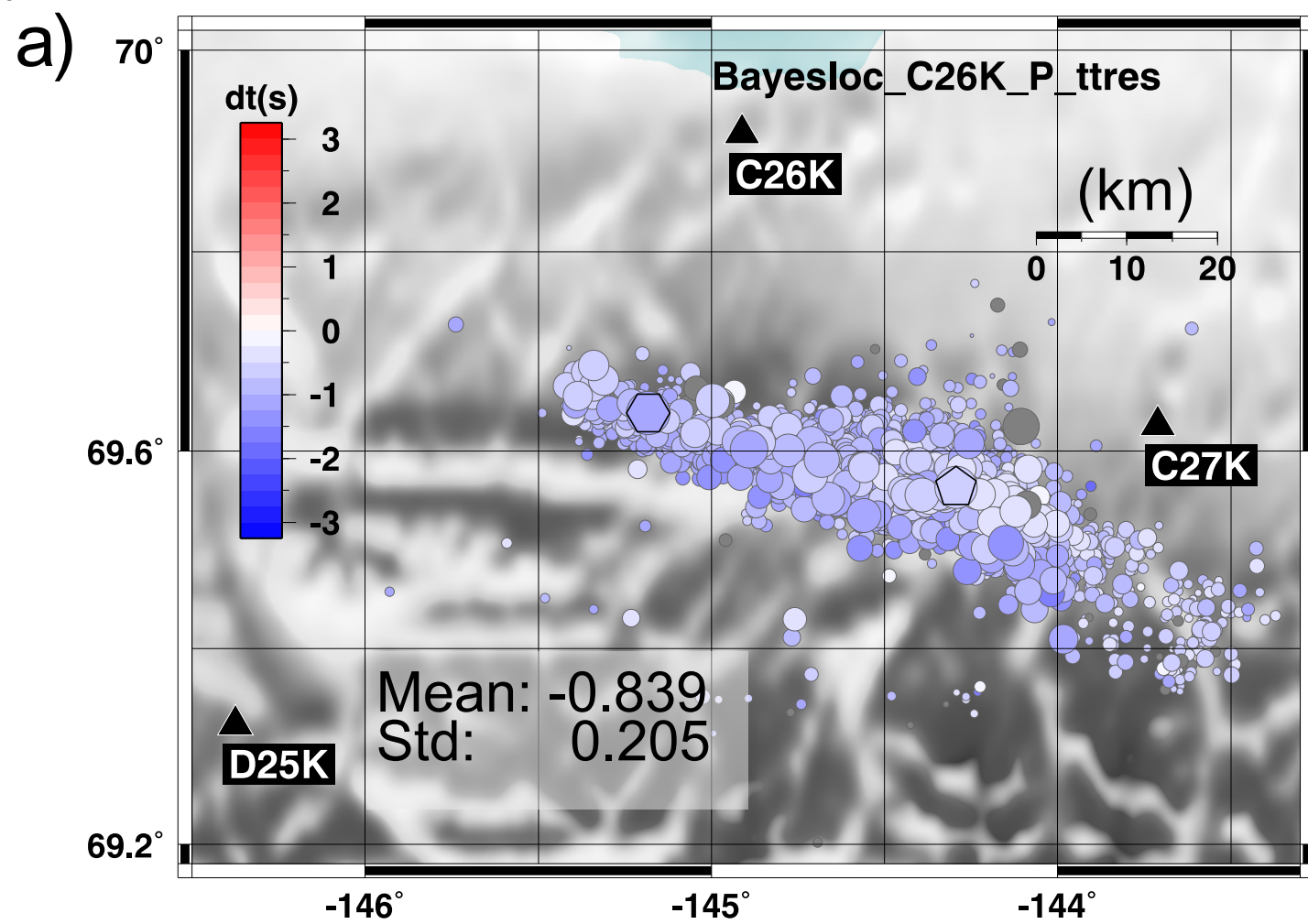


Figure 6

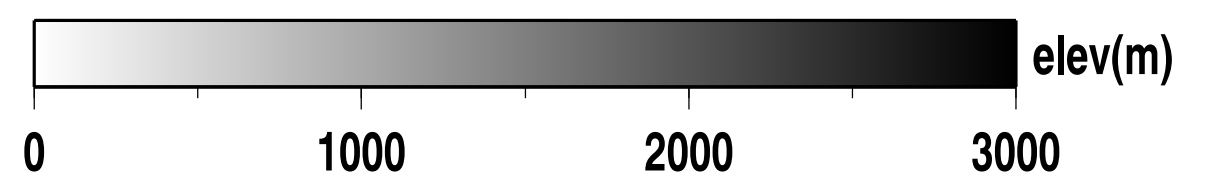
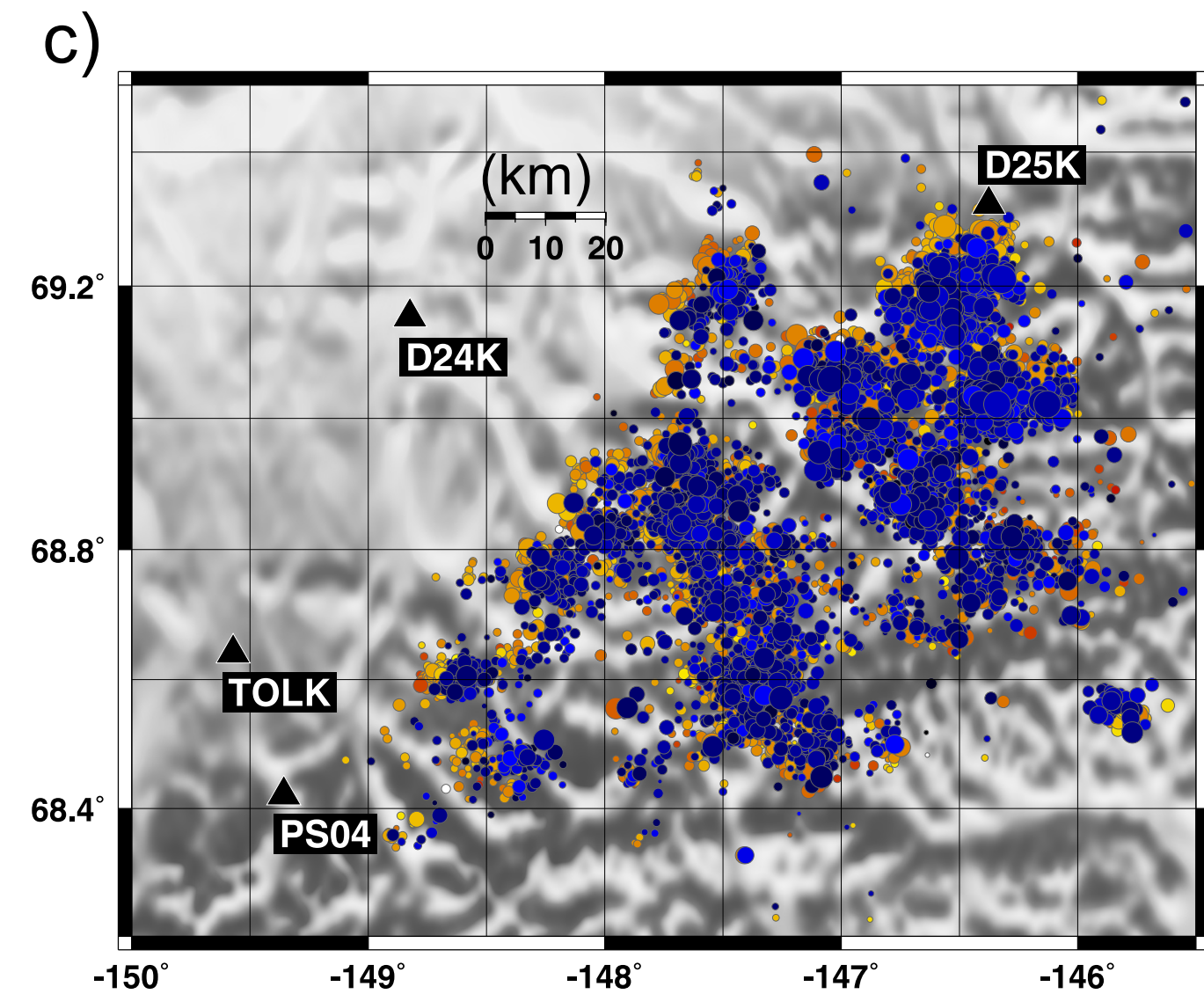
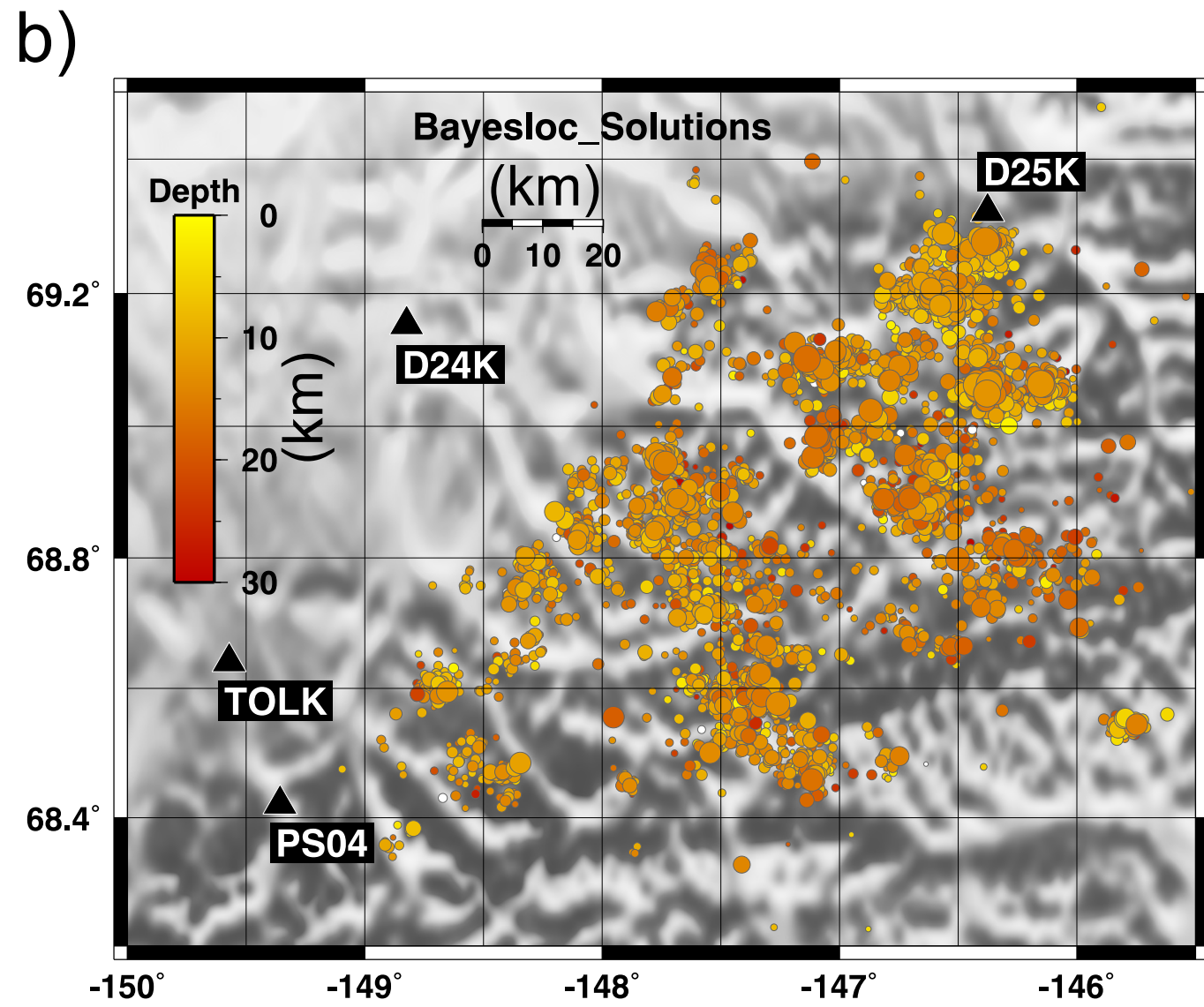
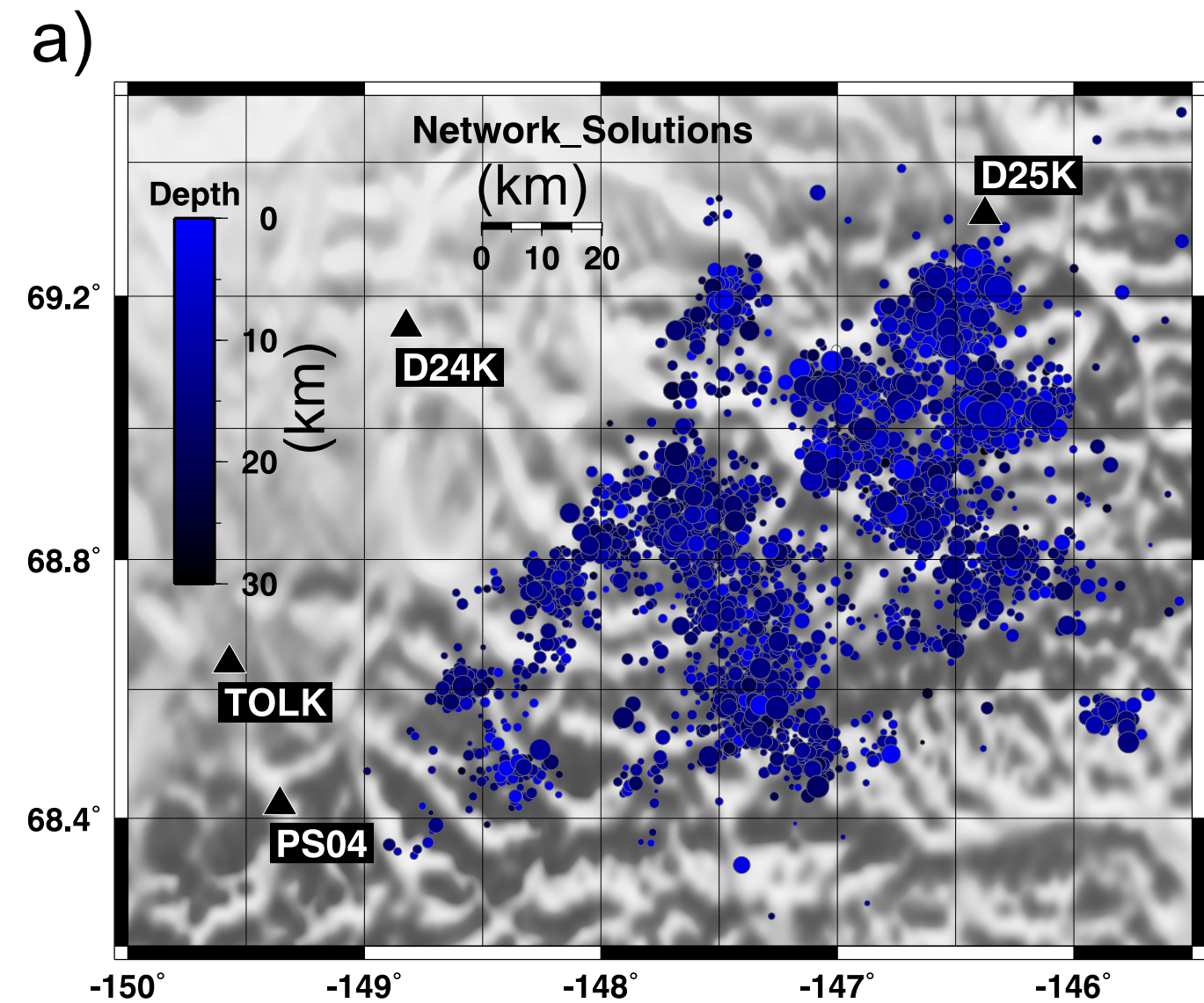


Figure 7

